Empirical pseudopotential method with nonspherical passivants for the atomistic study of silicon nanostructures

J. R. Cárdenas*
Programa de Física, Universidad del Atlántico, Puerto Colombia 081007, Atlántico, Colombia

(Received 28 June 2018; published 30 July 2018)

Atomistic calculations of passivated nanostructures remain difficult due to the computational demands related to the high number of atoms to be typically considered. The empirical pseudopotential method (EPM) offers a good alternative in this sense, but finding trustable pseudopotentials for passivants in this method is still elusive. Following the idea of extracting nonspherically symmetric potentials from density functional theory (DFT) calculations, hydrogen pseudopotentials for silicon passivation are derived here and used to calculate the electronic states of low-dimensional structures within the EPM scheme. The single-particle Schrödinger equation is solved with the ensuing pseudopotentials for slabs with surfaces on the (111), (110), and (100) planes, as well as for passivated quantum dots and wires of different size. In all cases, the band gap is traced as a function of the sample size, showing good convergence towards the bulk value. For the slabs, the surface local density of states is also calculated and compared successfully to experiments. The derivation of the nonspherical pseudopotentials is based on an analytic formulation of the crystal potential and its connection to a series of DFT calculations, resulting in reliable, highly transferable and first-principles based passivant pseudopotentials to be used with the EPM.

DOI: 10.1103/PhysRevB.98.045308

I. INTRODUCTION

Different features of semiconductor nanostructures are the basis of an increasing collection of potential applications in the field of nanotechnology, all intending to exploit the quantum confinement effects that nanostructures exhibit due to their reduced dimensions. This includes, for example, quantum information and quantum computation processes with quantum dots [1–5], solar cells [6,7], field effect transistors [8], high-performance light miters [9], and sensors of biological and chemical species [10].

In a wide range of these semiconductor-based potential devices, the surface of the nanostructure plays a significant role, as for example the case of colloidal systems [11]. At the nanoscale, the surface to bulk atoms ratio may be considerable and can therefore highly affect the electronic eigenvalues of the system. In this sense, an appropriate consideration of the surface in the theoretical calculations is of fundamental relevance to be able to accurately consider the surface effects.

The local version of the empirical pseudopotential method (EPM) [12–14] has been successfully and widely used to theoretically study different phenomena in the field of semiconductor physics. In this method, spherically symmetric potentials are used to construct and solve the single-particle Hamiltonian of a system, and the ensuing wave functions used to calculate different physical properties. The main achievement of the EPM is the lower computational cost in comparison to more elaborated techniques like, for example, density functional theory (DFT), since the electronic density does not have to be optimized, omitting the self-consistent cycles needed to minimize the total energy. Besides, within the EPM, the eigenvalues spectrum can be restricted by specialized diagonalization techniques to regions near the optical band gap [15], where the states mainly involved in the optical and transport properties of the nanostructures are located, avoiding the calculation of the whole spectrum from the ground state.

Depending on the size of the system, the electronic structure of semiconductor nanostructures can be treated with different methods [16]. For the very small systems comprehending up to few hundreds atoms, first-principles techniques like DFT or quantum Monte Carlo can be employed providing accurate results, but despite the sophistication of these methods, they become rapidly inefficient for bigger nanostructures, which can be composed for some millions atoms. At the opposite side in terms of the sample size, we can list mean-field theories such as the $\boldsymbol{k}\cdot\boldsymbol{p}$ and the envelope function model. Here, the rapid oscillations of the atomic structure are averaged to construct a continuum well behaved potential, and the kinetic energy is parametrized by an effective mass in such a way that the parabolicity of the band extremes of the bulk system are properly reproduced [17].

The empirical pseudopotential method seats between the first principles and the mean-field techniques, where the systems treated contain from few thousands to millions atoms [18]. In this regime, first-principles methods become inefficient because of the computational demands due to the number of atoms, and mean-field methods can miss predominant effects coming from the atomic structure.

In the EPM, the total screened crystal potential $V(\boldsymbol{r})$ is approximated by a superposition of atomic pseudopotentials $v(|\boldsymbol{r}|)$ centered at the atom positions $\boldsymbol{R}_n$,

$$V(\boldsymbol{r}) = \sum_{n}^{N} v(|\boldsymbol{r} - \boldsymbol{R}_n|)\,, \tag{1}$$

*jairocardenas@mail.uniatlantico.edu.co

where N is the total number of atoms and it has been assumed for simplicity that there is only one type of atom in the system. A main characteristic of the method is that the pseudopotentials used are spherically symmetric and hence completely real in reciprocal space. Considering that there is only one atom type, by Fourier transforming Eq. (1), the crystal potential in reciprocal space $V(\boldsymbol{G})$ can be written as [19,20]

$$V(\boldsymbol{G}) = \sum_{\alpha} \mathrm{e}^{-i\boldsymbol{G}\cdot\boldsymbol{R}_{\alpha}} v_{\alpha}(\boldsymbol{G}) \,, \tag{2}$$

with

$$v_{\alpha}(\boldsymbol{G}) = \frac{1}{\Omega_c} \int_{\infty} v_{\alpha}(\boldsymbol{r}) \mathrm{e}^{-i\boldsymbol{G}\cdot\boldsymbol{r}} \, \mathrm{d}^3\boldsymbol{r} \,, \tag{3}$$

where the $v_{\alpha}(\boldsymbol{G})$ are adjusted to fit experimental known values or *ab initio* calculations. Notice here that in real space the total and atomic potentials are real quantities, but that they can be complex in reciprocal space. In particular, since the bulk atomic pseudopotentials are considered as spherically symmetric, they are real in both, the real and reciprocal space.

Under this approximation, the EPM has been used for long time providing accurate results in bulk systems, but the situation is not the same in the case of passivated systems, where the atomic structure is truncated and the dangling bonds have to be passivated somehow. Distinct routes have been employed to generate passivants for different semiconductor compounds, but the main criteria to establish the pseudopotentials is that the energy gap of a given nanostructure is higher than the energy gap of the bulk system and/or the unlikely surface states are removed from the band gap [21,22].

The passivant pseudopotentials for the EPM so far reported keep the spherical symmetry of the bulk atoms, they are commonly fitted to a symmetric function like, for example, a series of Gaussians where the widths, amplitudes, and centers are adjusted until getting acceptable results [21,23,24]. This approximation is not accurate for passivants since there are dipole-moments induced due to charge transfer processes, all over the surface where the dangling-bonds are passivated, and the EPM does not take care of charge transfer phenomena intrinsically.

Passivant pseudopotentials without spherical symmetry for the semiempirical pseudopotentials method (SPEM) [25] have been recently generated and their accuracy demonstrated by comparison to DFT calculations [20]. The semiempirical potentials are distinct from the local empirical potentials in the sense that the former separates the atomic potential into a local and a nonlocal part, where the nonlocal part is angular momentum dependent. By going beyond the spherical approximation, the charge transfer phenomena at the surface are introduced into the calculations and, therefore, the related electric dipoles are reproduced in good approximation. It also means that the passivants have to be included as complex pseudopotentials (CPSPs) in reciprocal space, since they are not symmetric anymore in real space [20], in contrast to the bulk atoms that are described by fully real pseudopotentials in real and reciprocal space.

Following the same ideas, the method to generate CPSPs is extended in this work to be implemented in the empirical pseudopotential method, and used to extract passivant pseudopotentials for silicon. The procedure is based on an analytic and straightforward formulation that relates the atomic potentials and positions to the total crystal potential of a couple of carefully chosen samples. The basic idea of the method is as follows: (i) to take the crystal potential of two different passivated slabs of the same material calculated with DFT and the local density approximation (LDA), (ii) to use the calculated total potentials and the atomic bulk pseudopotentials as input for the analytic formulation, (iii) to solve a system of equations to extract the real and imaginary parts of the complex passivant pseudopotentials, and (iv) to fine adjust the CPSP in order to match the convergence of the energy gap to the bulk value and remove possible surface states from the band gap [21,22].

It is worth clarifying three aspects of the procedure described above: first, the method needs two components to work—the LDA-DFT calculated total crystal potential and the atomic potentials (previously known) of the host system to be passivated, and these two components must correspond in order to include an appropriate band offset in the resulting CPSP. Second, the methods needs two total crystal potentials for the case of binary systems, since there are two different passivants to treat, but if the host system is composed by only one atom, only one total crystal potential in enough. Third, the final adjustment (tuning) must be very small so that the *ab initio* characteristics of DFT are conserved.

In the last part of this work, a hydrogen-based CPSP for silicon is derived and used to calculate the electronic structure of different systems. First of all, the band gap of silicon slabs with orientations along the [111], [110], and [100] directions is presented, since these calculations were used to tune the CPSP and ensure the convergence to the bulk value. Subsequently, the energy band gap of quantum wires (QWs) and dots (QDs) is traced as a function of the sample size. In this part, realistic rounded structures are used; there are reports of this kind of studies using the EPM, but based on rather fanciful squared shapes (probably to keep the same surface face over the whole sample) and always using spherically symmetric passivant potentials [26–28], and some others using more feasible structures are based in methods that require robust computational facilities [29,30]. Finally, the surface local density of states (LDOS) is calculated for the slabs and compared to ultraviolet-photoemission spectroscopy (UPS) measurements [31], and the EPM wave functions compared to DFT, in both cases showing a good correlation.

II. PASSIVANT PSEUDOPOTENTIAL GENERATION FOR THE EPM

A. Method

Even if the pseudopotentials extracted here are intended to passivate silicon nanostructures, the methodology introduced is presented in a general formalism, in such a way that it can be applied to extract passivant pseudopotentials for binary systems too. It means that for silicon only one total crystal potential is required, but the following description is delineated in terms two crystal potentials of different structures.

As mentioned before, to start the process, we need to have the atomic potentials of the host system and the total crystal potential of two different passivated slabs [$V^{(1)}$ and $V^{(2)}$] of the

same material. Consequently, the slabs have different number of atoms, but they have to be contained in supercells of the same size in order to have coincidence between the G-point grids in reciprocal space [20]. There is no restriction about the orientation of the slabs, but the [111] direction is chosen here, in particular, for symmetry reasons that will be clarified later. The potentials are expected to be effective potentials of the crystals, including all the interactions of a single electron with the environment. In this work, we use density functional theory [32], with the local density approximation, to get the $V^{(1)}$ and $V^{(2)}$ in concordance with the bulk atomic pseudopotential of the host system [19,20].

Interpreting the total potential as the superposition of atom centered pseudopotentials, we can write the potential $V^{(j)}$ of each one of the slabs (j) as

$$V^{(j)}(\boldsymbol{r}) = \sum_{\alpha}^{N_{\rm sp}} \sum_{n}^{N_{\alpha}^{(j)}} v_{\alpha}(\boldsymbol{r} - \boldsymbol{R}_{\alpha,n}) \,, \tag{4}$$

where the number of species $N_{\rm sp}$ is the same for both slabs, but the number of atoms N_{α} of each specie α is different. Applying a Fourier transformation in the same manner done in Eq. (2), we can write

$$V^{(j)}(\boldsymbol{G}) = \sum_{\alpha}^{N_{\rm sp}} \sum_{n}^{N_{\alpha}^{(j)}} \mathrm{e}^{-i\boldsymbol{G}\cdot\boldsymbol{R}_{\alpha,n}^{(j)}} v_{\alpha}(\boldsymbol{G}) \tag{5}$$

or

$$V^{(j)}(\boldsymbol{G}) = \sum_{\alpha}^{N_{\rm pas}} \sum_{m}^{N_{\alpha}^{(j)}} \mathrm{e}^{-i\boldsymbol{G}\cdot\boldsymbol{R}_{\alpha,m}^{(j)}} v_{{\rm pas},\alpha}(\boldsymbol{G}) + \sum_{\alpha}^{N_{\rm bulk}} \sum_{n}^{N_{\alpha}^{(j)}} \mathrm{e}^{-i\boldsymbol{G}\cdot\boldsymbol{R}_{\alpha,n}^{(j)}} v_{{\rm bulk},\alpha}(\boldsymbol{G}) \,, \tag{6}$$

where the passivant atomic potentials ($v_{{\rm pas},\alpha}$) have been separated from the bulk part ($v_{{\rm bulk},\alpha}$). The term of interest in the last equation is the first summation on the right-hand side, which is the unknown part. The second summation can be reproduced since the atom positions and the bulk spherical pseudopotentials are known. The $V^{(j)}(\boldsymbol{G})$ can be found from the Fourier transform of the total potentials in real space previously calculated with DFT,

$$V^{(j)}(\boldsymbol{G}) = \frac{1}{\Omega_c} \int_{\Omega_c} V^{(j)}(\boldsymbol{r}) \mathrm{e}^{-i\boldsymbol{G}\cdot\boldsymbol{r}} \, \mathrm{d}^3\boldsymbol{r} \,. \tag{7}$$

In this point, we take into account the fact that the passivant pseudopotentials are not spherically symmetric. Therefore the $v_{{\rm pas},\alpha}(\boldsymbol{G})$ have a symmetric real and an antisymmetric imaginary part in reciprocal space. Defining the next function to explicitly separate the passivant pseudopotentials components

$$\gamma^{(j)}(\boldsymbol{G}) = (\mathrm{Re}[v_{{\rm pas},a}] + i\,\mathrm{Im}[v_{{\rm pas},a}]) S_a^{(j)}(\boldsymbol{G}) + (\mathrm{Re}[v_{{\rm pas},c}] + i\,\mathrm{Im}[v_{{\rm pas},c}]) S_c^{(j)}(\boldsymbol{G}) \,, \tag{8}$$

where

$$S_a^{(j)}(\boldsymbol{G}) = \sum_{m}^{N_{{\rm pas},a}^{(j)}} \mathrm{e}^{-i\boldsymbol{G}\cdot\boldsymbol{R}_{a,m}^{(j)}} \,, \tag{9}$$

$$S_c^{(j)}(\boldsymbol{G}) = \sum_{m}^{N_{{\rm pas},c}^{(j)}} \mathrm{e}^{-i\boldsymbol{G}\cdot\boldsymbol{R}_{c,m}^{(j)}} \,, \tag{10}$$

we can rewrite Eq. (6) in the form

$$\gamma^{(j)}(\boldsymbol{G}) = V^{(j)}(\boldsymbol{G}) - \sum_{\alpha}^{N_{\rm bulk}} \sum_{n}^{N_{\alpha}^{(j)}} \mathrm{e}^{-i\boldsymbol{G}\cdot\boldsymbol{R}_{\alpha,n}^{(j)}} v_{{\rm bulk},\alpha}(\boldsymbol{G}) \,, \tag{11}$$

where it has been considered that there are two kind of passivants, one for the anions ($v_{{\rm pas},a}$) and one for the cations ($v_{{\rm pas},c}$).

At this stage, we can clarify why we need to have the total potentials of two different slabs ($V^{(j)}$): Eq. (8) comprises four unknowns (the real and imaginary part of each passivant) and two equalities (the real and the imaginary part of the equation), if we write the same equation for two different slabs, we complete a system of four unknowns and four equalities, making the system solvable. This also explains why we need only one total crystal potential if the system is composed by only one bulk atom and, therefore, only one passivant.

A main difference here with respect to the SEPM and the effective passivants potentials described in Ref. [20] is the reconstruction of the bulk-atom contribution to the total potential. In the SEPM, the pseudopotentials are divided into a local and a nonlocal part and the method is used to extract only the local part of the potential, here we work with the total crystal potential and hence the passivant potentials generated are also total atomic potentials suited for the EPM.

Writing together Eq. (8) for each slab, the ensuing system of equations can be expressed in a matrix form as

$$\begin{pmatrix} \mathrm{Re}[S_a^{(1)}(\boldsymbol{G})] & -\mathrm{Im}[S_a^{(1)}(\boldsymbol{G})] & \mathrm{Re}[S_c^{(1)}(\boldsymbol{G})] & -\mathrm{Im}[S_c^{(1)}(\boldsymbol{G})] \\ \mathrm{Im}[S_a^{(1)}(\boldsymbol{G})] & \mathrm{Re}[S_a^{(1)}(\boldsymbol{G})] & \mathrm{Im}[S_c^{(1)}(\boldsymbol{G})] & \mathrm{Re}[S_c^{(1)}(\boldsymbol{G})] \\ \mathrm{Re}[S_a^{(2)}(\boldsymbol{G})] & -\mathrm{Im}[S_a^{(2)}(\boldsymbol{G})] & \mathrm{Re}[S_c^{(2)}(\boldsymbol{G})] & -\mathrm{Im}[S_c^{(2)}(\boldsymbol{G})] \\ \mathrm{Im}[S_a^{(2)}(\boldsymbol{G})] & \mathrm{Re}[S_a^{(2)}(\boldsymbol{G})] & \mathrm{Im}[S_c^{(2)}(\boldsymbol{G})] & \mathrm{Re}[S_c^{(2)}(\boldsymbol{G})] \end{pmatrix} \begin{pmatrix} \mathrm{Re}[v_{{\rm pas},a}(\boldsymbol{G})] \\ \mathrm{Im}[v_{{\rm pas},a}(\boldsymbol{G})] \\ \mathrm{Re}[v_{{\rm pas},c}(\boldsymbol{G})] \\ \mathrm{Im}[v_{{\rm pas},c}(\boldsymbol{G})] \end{pmatrix} = \begin{pmatrix} \mathrm{Re}[\gamma^{(1)}(\boldsymbol{G})] \\ \mathrm{Im}[\gamma^{(1)}(\boldsymbol{G})] \\ \mathrm{Re}[\gamma^{(2)}(\boldsymbol{G})] \\ \mathrm{Im}[\gamma^{(2)}(\boldsymbol{G})] \end{pmatrix} . \tag{12}$$

In deriving the last set of equations, special care has to be taken with the imaginary component of the passivants, since they are antisymmetric. They suffer a reflection depending on whether they are on the right or left surface of the slab [20], consequently minus signs appear in some terms during the derivation.

The real and imaginary components of the passivant pseudopotentials can finally be extracted by numerically solving Eq. (12). The matrix term depends only on the structure factors and, hence, depends solely on the atom positions. The vector at the left-hand side contains the wanted quantities. The vector at the right-hand side can be computed using Eq. (11) from

the atomic bulk pseudopotentials and the $V^{(j)}$ from the DFT calculations. It is worth mentioning that Eq. (12) has to be solved for each $\boldsymbol{G}$ vector, justifying that the sample slabs must be contained in supercells of the same size, so that the corresponding reciprocal space $\boldsymbol{G}$-point grids match for the representation of the $V^{(j)}$.

Even though the derivation of Eq. (12) is exact, the spherical approximation is still present in the bulk EPM pseudopotentials, and this introduces some scatterers on the extracted passivant pseudopotential, which has to be removed during the process as will be shown later. These scatterers have a well-defined periodicity since they originate from the difference between the real atomic potential and the spherically symmetric approximated EPM pseudopotentials in Eq. (11) and, hence, have the atom position periodicity.

B. Implementation of the passivant nonspherical pseudopotentials in the EPM

Before continuing with the application of the method to derive CPSPs, here, we will outline how the nonspherical pseudopotentials can be implemented into the EPM and comment on the election of the [111] orientation of the slabs as a reference system to extract the potentials.

The real and imaginary components of the passivants need to be implemented in the total single-particle Hamiltonian separately. In the case of the real parts, they can simply be added up like normal bulk potentials because they have the same symmetry. The imaginary components need, however, to be set depending on the surface orientation to properly reproduce the dipole moments formation.

The (111) surface offers the possibility of having the passivated bond along the [111] directions, it means perpendicular to the surface plane. In such a condition and for symmetry reasons, we can expect that the passivant potential gets its maximum absolute value along the direction of the bulk-passivant bond in reciprocal space and, since the potential is antisymmetric, it should become zero for a $\boldsymbol{G}$ vector on the (111) plane.

Based on the previous analysis, we can establish a route to implement the complex components of the passivant pseudopotentials into the EPM. First, we extract the passivant using the (111) surface and the bulk-passivant bond perpendicular to it, in order to guarantee that the pseudopotential extracted corresponds to its maximum absolute value; this explains the election of this slab in particular as mentioned in the introduction. Second, we project the potentials in reciprocal space for the required $\boldsymbol{G}$ vectors, in such a way that it becomes zero on the surface and reflected across it.

With these considerations, the total potential of a given passivated system can be now written as

$$\begin{aligned} V(\boldsymbol{G}) = & \sum_{\alpha}^{N_{\text{bulk}}} v_{\text{bulk},\alpha}(|\boldsymbol{G}|) \sum_{n}^{N_\alpha} \mathrm{e}^{-i\boldsymbol{G}\cdot\boldsymbol{R}_{\alpha,n}} \\ & + \sum_{\alpha}^{N_{\text{pas}}} \mathrm{Re}[v_{\text{pas},\alpha}(|\boldsymbol{G}|)] \sum_{n}^{N_\alpha} \mathrm{e}^{-i\boldsymbol{G}\cdot\boldsymbol{R}_{\alpha,n}} \\ & + \sum_{\alpha}^{N_{\text{pas}}} \mathrm{Im}[v_{\text{pas},\alpha}(|\boldsymbol{G}|)] \sum_{n}^{N_\alpha} \mathrm{e}^{-i\boldsymbol{G}\cdot\boldsymbol{R}_{\alpha,n}} \cos(\theta_{\alpha,n}), \end{aligned} \tag{13}$$

where $\theta_{\alpha,n}$ is the angle between the directional vector $\boldsymbol{p}_{\alpha,n}$ perpendicular to the system surface, at the position of each passivant, and the $\boldsymbol{G}$ vector, so that

$$\cos(\theta_{\alpha,n}) = \frac{\boldsymbol{p}_{\alpha,n}\cdot\boldsymbol{G}}{|\boldsymbol{p}_{\alpha,n}||\boldsymbol{G}|}\,. \tag{14}$$

When writing Eq. (13), we imply that the vectors $\boldsymbol{p}_{\alpha,n}$ have to be set for each passivant depending on its position on the sample surface and according to the sense in which the CPSPs are generated. More clearly, they have to be perpendicular to the nanostructure surface so that the imaginary component of the CPSP is properly reflected across the surface, but if they are pointing outwards or inwards, the nanostructures have to be correlated with the CPSP generation; if it is performed going outwards or inwards the structure in reciprocal space, respectively [20].

C. Generation of CPSP for Si

Notice that here we have dealt with the total LDA potential, for this reason, the CPSPs are generated using a silicon effective atomic pseudopotential previously derived [19], because of the binding to DFT. For the fine tuning of the CPSP and all the postgeneration calculations, the EPM accepted Si pseudopotential reported in Ref. [18] is used. In this way, we not only avoid proposing a new Si empirical pseudopotential, but we also ensure that the bulk properties (band structure, effective masses, and work function) are already corrected to the experimental values. The Si potential was renormalized to the unit cell volume rather than to the number of atoms, in order to allow for the proper inclusion of the vacuum space when treating the passivated systems and to have the CPSP and bulk PSP normalized on the same basis. After these considerations, the Si empirical pseudopotential (measured in hartree $\times$ bohr^3) used was

$$V_{\text{Si}}(G) = \frac{a_1(G^2 - a_2)}{a_3\exp(a_4 G^2) - 1}\,, \tag{15}$$

where $a_1 = 36.317$, $a_2 = 2.19$, $a_3 = 2.06$, and $a_4 = 0.487$.

Since for pure Si there is only one type of bulk atom to passivate, the process could be performed with only one total potential in Eq. (12). However, in order to keep a general formalism, the derivation here is done with the total potential of two different slabs: Si_8H_4 and $Si_{12}H_4$, both in a $40\sqrt{3}a_{\text{LDA}}$ long supercell, using a relaxed LDA lattice constant of $a_{\text{LDA}} = 5.478$ Å, and the relaxed H-Si bond length of 1.433 Å to guarantee that the calculations are performed in the structural equilibrium state.

The real and imaginary parts of the silicon passivant pseudopotential are shown in Fig. 1 as extracted with Eq. (12) from the DFT results. It is clear that the imaginary component is not negligible in comparison to the real part, indicating that it must play an important role in calculations and should not be disregarded. Besides, the imaginary component becomes more and more important, exceeding the real component by one order of magnitude, as G approaches zero. This strongly supports the importance of the imaginary part of the CPSPs in calculations, since the small G region is related to the long-range interaction and, hence, it is responsible for the

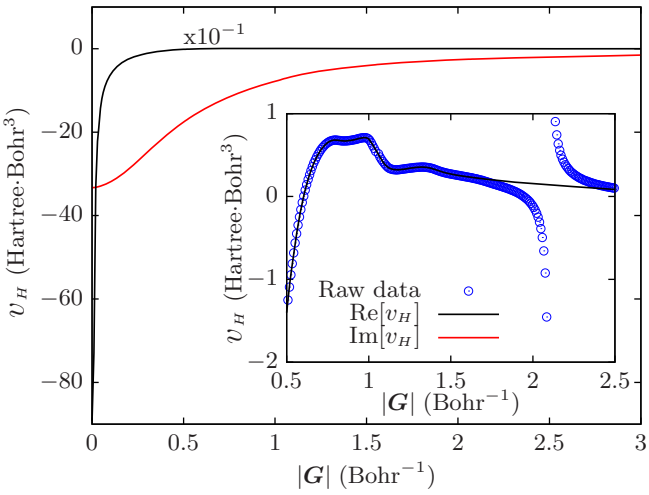

FIG. 1. Real and imaginary components of the passivant pseudopotential (v_H) for silicon as a function of the magnitude of the $\boldsymbol{G}$ vector. The inset shows a discontinuity on the raw data (as extracted from DFT) and how the interpolation passes through it.

band offset in heterostructures and strongly influences the distribution of energy eigenvalues [19].

The inset in Fig. 1 shows a segment of the imaginary component where the continuous potential is traced by a spline interpolating through the discontinuity in the original DFT data (raw data), disregarding the points that are clearly out of the tendency as was mentioned in Introduction. We can also notice that the imaginary component shows some wiggles that make it impractical to fit the curve to a superposition of Gaussian functions as customary done, since the number of Gaussians required becomes too high. Nevertheless, work is in progress pointing in this direction, and the fitted CPSP will be reported in a future report. To the contrary, the real component is rather smooth showing a typical shape for these kind of potentials.

The fine tuning of the CPSP is performed in such a manner that the energy band gap of long slabs converges to the experimentally accepted value of 1.178 eV for the bulk system. This process is the only empirical modification on the

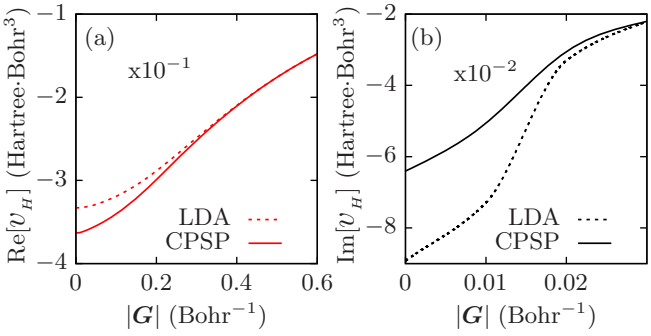

FIG. 2. Empirical tuning on the long-range interaction of the (a) real and (b) imaginary components of the extracted hydrogen passivant pseudopotential (v_H) for silicon. The real and imaginary components are multiplied, respectively, by a factor of 10^{-1} and 10^{-2} for better comparison.

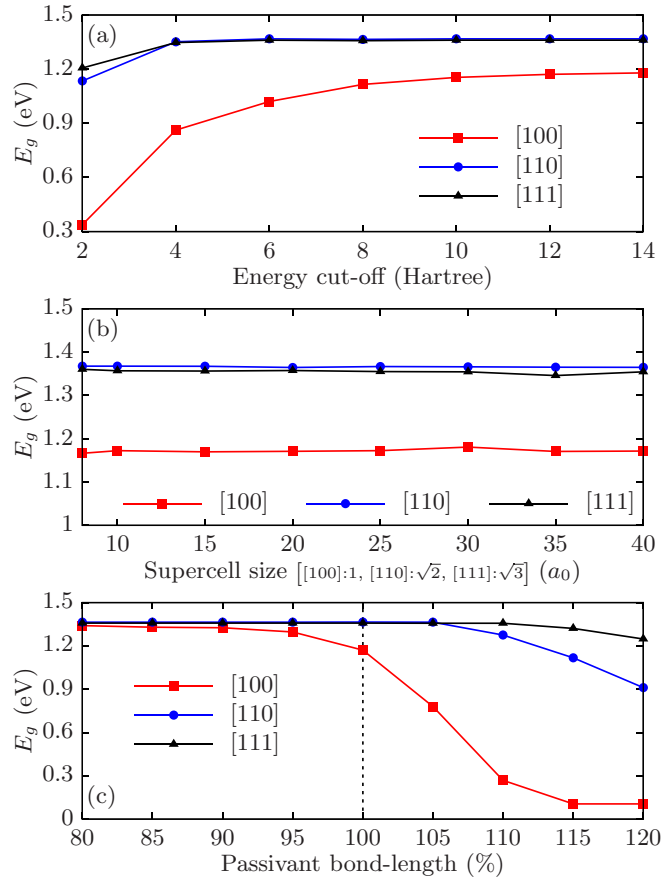

FIG. 3. (a) Energy gap converge with the cutoff energy for slabs along the [111], [110], and [100] directions. (b) Stability of the eigenvalues for the same atomic structure but for different supercell sizes: for each supercell, the G point grid is different. Notice that the horizontal axis is scaled by a factor of 1, $\sqrt{2}$, and $\sqrt{3}$ for the [100], [110], and [111] directions, respectively. (c) Influence of the Si-H bond length on the energy gap using the equilibrium bond length as a reference. In each panel, the length of the slabs corresponds to six unit cells according to the respective direction.

pseudopotentials and happens to be a small shift over only a small region along the first G points as shown in Fig. 2. In this stage and for all the subsequent calculations and results, the Si empirical pseudopotential of Eq. (15), the hydrogen CPSP extracted here, the experimental Si lattice constant of $a_o = 5.431$ Å, and the accepted value of the Si-H bond-length of 1.42 Å are used.

To track the convergence of the energy gap to the bulk value, a minimization procedure [33,34] was performed simultaneously with slabs of different size and elongated along the [100], [110], and [111] crystallographic directions. In this way, the CPSP is tuned to fit different kind of surfaces all together, guaranteeing a high level of transferability and, therefore, the capability of using the same passivant pseudopotential to study systems of any shape with accurate results.

Comparing the shifts of the real and imaginary parts, we notice that the correction is much stronger in the imaginary component, but it occurs only over the extreme small $|\boldsymbol{G}|$ values, going approximately up to $G = 0.04$ bohr^{-1}, one order of magnitude less in relation to the real component, where the

correction reaches the $G = 0.4$ bohr^{-1} value approximately. For higher $\boldsymbol{G}$ values, the CPSP is left as extracted from the LDA-DFT calculations. The need to adjust the CPSP only in the small G region is expected since the Si pseudopotential of Eq. (15) is constructed empirically to reproduce bulk properties, where only few G points are needed and none smaller than the one corresponding to the bulk system [18,19].

Different aspects concerning convergence are compiled in Fig. 3, in each case, slabs of length equivalent to six unit cells according to the crystallographic directions are used, this means: $6a_o$, $6\sqrt{2}a_o$, and $6\sqrt{3}a_o$ for the [100], [110], and [111] directions, respectively. First of all, the convergence of the band gap is plotted as a function of the energy cutoff used in the plane-wave expansion. The [111] and [110] slabs show a faster convergence, both presenting little deviation starting from around 4 Ha [Fig. 3(a)]. In the case of the [100] slab, the convergence requires a higher energy cutoff of 8 Ha approximately. This behavior is expected since the [111] slab was the system used to extract the CPSP and it is reasonable to expect the best behavior for this orientation.

The transferability of the CPSP in relation to the supercell size is demonstrated in Fig. 3(b), where the size of the material slabs has been kept constant while different vacuum spaces were used. This combination of different supercell sizes for the same atomic structure leads to calculations spanned by different sets of G points that should converge to the same eigenvalues. In particular, when the supercell gets bigger, the G points grid gets denser. The results shown in Fig. 3(b) proves the stability of the CPSP since the band gap values for each slab deviate very little as the supercell becomes bigger.

The energy band gap of the same slabs but for a different Si-passivant bond length is shown in Fig. 3(c). This is an important study in order to know the attention that needs to be paid to the passivant position over the structure. Besides, it has been pointed out that the electronic structure of hydrogen passivated Si quantum systems can be highly affected by the surface structure [28,30]. Examining the results shown in Fig. 3(c), we can conclude that the passivant position affects more strongly the electronic structure when the bond length exceeds the corresponding equilibrium position than in the case where the Si-passivant bond is shorter. Besides, the (100) face shows a stronger influence on the electronic structure, which can be explained by the fact that when the Si-H bond length is enlarged on the (100) surface, the H-H distance becomes shorter, enhancing the dipole moments at the surface and, therefore, influencing the total confining potential of the nanostructure more strongly.

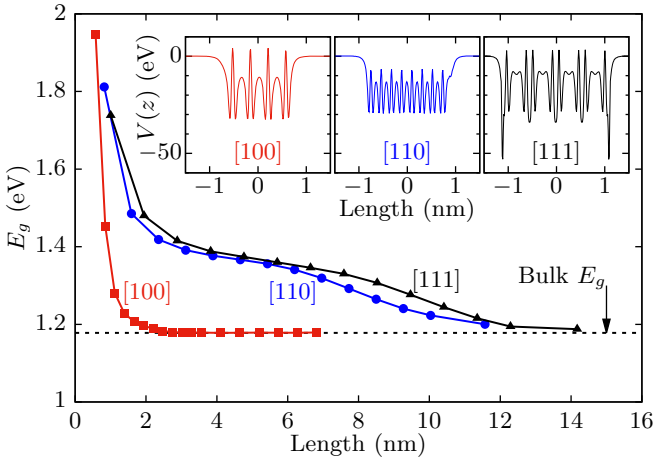

FIG. 4. Energy band gap for Si slabs along the [100], [110], and [111] directions as a function of the slab length. The E_g values converge to the experimental value of 1.178 eV. The insets show the local potential of nearly 2-nm-long slabs along each direction.

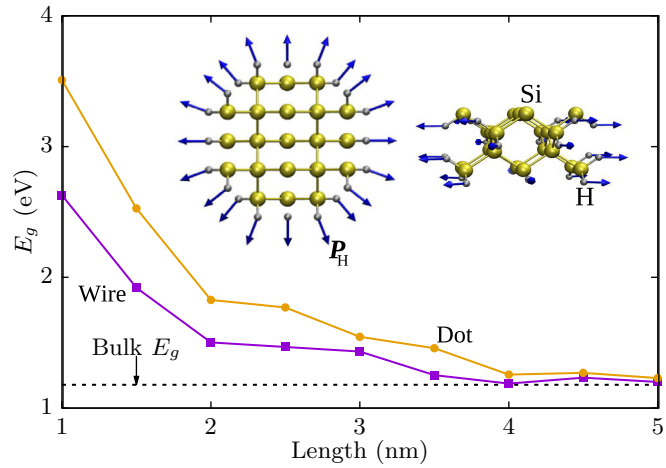

FIG. 5. Band gap energy for a Si quantum dot and a Si quantum wire ranging in both cases from 1 to 5 nm. The diagram illustrates the cross section of a quantum wire with the passivant vector $\boldsymbol{P_H}$ distribution over the surface.

III. PASSIVATED SILICON NANOSTRUCTURES

The slab calculations done to tune the DFT-LDA extracted complex potential are shown in Fig. 4, together with the profile of the local potential averaged over the in-plane direction.

TABLE I. Number of Si and H atoms of the QD and QW nanostructures in Fig. 5.

Structure	No. of Si	No. of H
1.0-nm QD	29	36
1.5-nm QD	87	76
2.0-nm QD	175	116
2.5-nm QD	389	196
3.0-nm QD	705	300
3.5-nm QD	1087	412
4.0-nm QD	1683	580
4.5-nm QD	2329	684
5.0-nm QD	3205	801
1.0-nm QW	21	20
1.5 nm QW	45	28
2.0-nm QW	89	44
2.5-nm QW	137	52
3.0-nm QW	193	60
3.5 nm QW	261	76
4.0-nm QW	341	84
4.5-nm QW	437	92
5.0-nm QW	525	100

First of all, we can notice how the band gap values converge smoothly to the bulk band gap simultaneously in all cases. It is worth keeping in mind that the same CPSP has been used in all calculations. The faster and more monotonous convergence of the [100] sample is due to its more uniform crystal potential (see the inset of Fig. 4) that would resemble more closely, when taking the mean value, the squared potential well of the effective mass models. The slower and less regular convergence of the [110] and [111] samples may be explained by the different shape of the local potential right at the barriers: the [110] slab has an asymmetric local potential due to the different distribution of passivant at both sides of the sample, and the [111] slab has very dip and narrow potential tips at the barriers, as can be noticed in the insets of Fig. 4.

The energy band gap of quantum wires and quantum dots as a function of the nanostructure diameter is shown in Fig. 5. The figure also shows a diagram of the passivant vectors ($\boldsymbol{P_H}$) distributed perpendicularly to the surface on each passivant site for a cross section of a QW. The rather fast convergence to the bulk energy gap is explained by the predominant [100] surface type [30] (an Si-H_2 phase), in comparison to Fig. 4. The QDs calculations were done with a cutoff energy of 5 Ha, while the QW calculations were done at 6 Ha, and with the axes along the [100] direction. The number of Si and H atoms for each structure are listed in Table I.

Results of the surface local density of states, defined as

$$\sigma(E) = \int_S \sum_i |\psi_i(\boldsymbol{r})|^2 \delta(E - E_i)\, \mathrm{ds}\,, \tag{16}$$

for planes parallel to the surface of the [111], [110], and [100] slabs calculated with the EPM are shown in Fig. 6, together with the experimental results of the UPS spectra of the (111) surface after Ref. [31]. The integral in Eq. (16) runs over the whole surface perpendicular to the axes of the slab, and has been calculated for three positions from the surface: the passivant and the outermost silicon layers, and the plane cutting the middle point between them (the H, Si, and H-Si label in Fig. 6, respectively). Figure 6 also shows the averaged LDOS over the firs unit cell in each case ($\sum_n \sigma_n$).

The comparison of the averaged theoretical LDOS to the experimental results shows a good agreement in the number and width of the peaks, suggesting that the photoemission of the UPS spectra is highly affected by the Si internal layers. The occurrence of a second peak arising from the Si-H bond in the vicinity below −9 eV in the (111) surface is also in agreement with other reports [31,35], where the little shift of

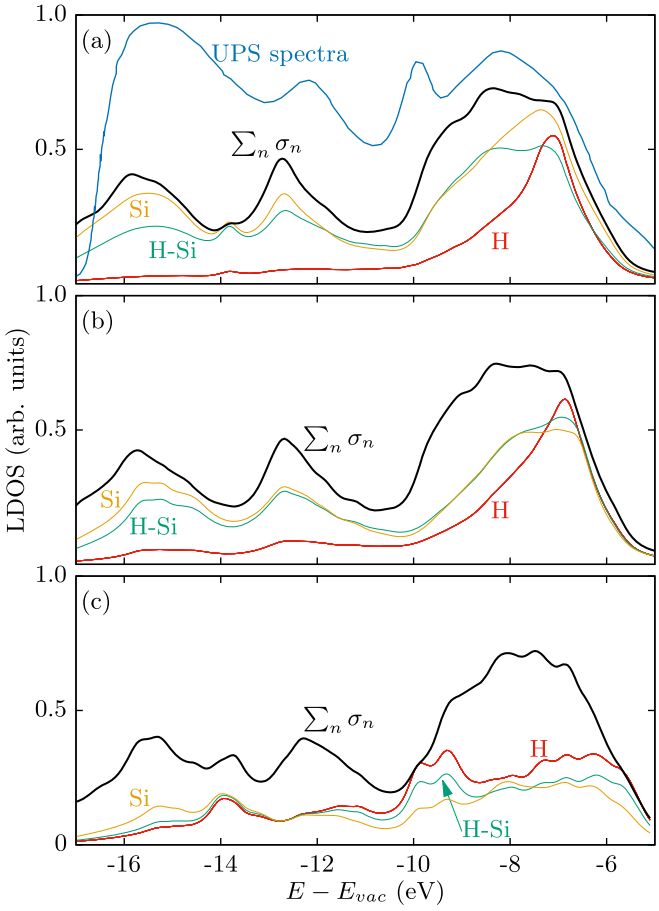

FIG. 6. Local density of states of the (a) [111], (b) [110], and (c) [100] slabs. H stands for the passivant surface layer, Si-H for the plane at the middle point between the Si-H bond, and Si for the first silicon layer. The summation of the LDOS over a unit cell from the surface ($\sum_n \sigma_n$) as well as the (111) experimental UPS spectra are also presented [31].

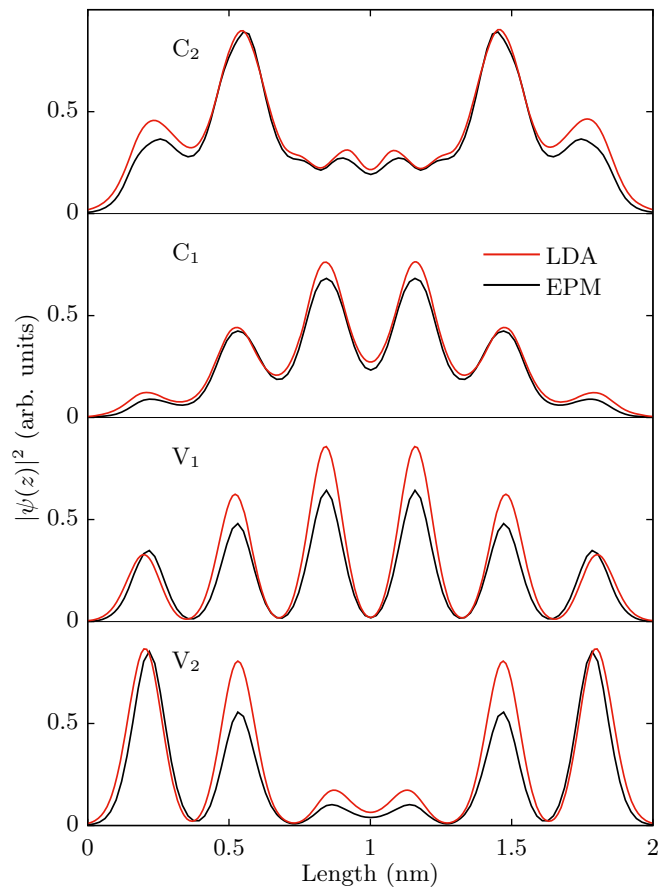

FIG. 7. Comparison of the DFT-LDA and the EPM-CPSP wave functions for a 2-nm-long slab. The squared wave functions are averaged along the transverse plane of the structure and corresponds to the first two conduction and first two valence states.

the second peak towards higher energy may be explained by the temperature conditions of the experiment [31] and the surface reconstruction phenomena that take place in experiments but were not considered in these calculations. The (111) and (110) surfaces are both characterized by a Si-H phase, while the (100) surface presents a Si-H_2 phase. This deference is reflected in the LDOS results, where the H curves in panels (a) and (b) of Fig. 6 are very similar and notably differ from the H curve in Fig. 6(c).

Finally, in Fig. 7, the EPM charge density is compared to DFT for a 2-nm slab in the [111] direction, where the first two conduction (C_i) and valence (V_i) wave functions are plotted. It is known that LDA-DFT fails to accurately predict energy band gap values [36], but that the wave-function symmetries and all valence states are well reproduced [29]. In these terms, a comparison to the LDA-DFT wave functions is a good benchmark to determine the accuracy of the CPSP in the scheme of the EPM. Figure 7 shows how the EPM calculations reproduce well the charge density distribution of the LDA-DFT, where the *s*- and *p*-type symmetries of the envelope wave functions, as well as the fast oscillations related to the atomic structure, are recognized.

IV. CONCLUSIONS

A method to generate passivant pseudopotentials with nonspherical symmetry to be employed within the empirical pseudopotential method was described. The method is based on an analytic formulation of the total crystal potential and is related to DFT in such a way that the derived CPSPs have LDA quality. Also, the ensuing pseudopotentials have real and imaginary components in reciprocal space, which allows for a proper consideration of charge transfer processes occurring at the surface of the nanostructures, which is an advantage over the common passivation methods in terms of spherical pseudopotentials.

The method was used to extract a hydrogen based CPSP for silicon and its accuracy and transferability are demonstrated with the calculation of different nanostructures: slabs, quantum wires, and dots, where the energy band gap in all cases converged to the bulk value for big samples. Besides, the surface local density of states was calculated reproducing experimental results. The final assessment of the CPSP is the close reproduction of DFT wave functions, where the localization and fast oscillations of the wave functions related to the atomic structure are well recreated.

This work supports the idea that the dipole moments at the surface of passivated nanostructures can be treated by the inclusion of nonspherically symmetric pseudopotentials into the EPM, and that it is of fundamental importance in order to have accurate results, since the imaginary component of the CPSP is not negligible in comparison to the real component, which alone would correspond to the spherical approximation.

[1] D. Loss and D. P. DiVincenzo, Phys. Rev. A **57**, 120 (1998).
[2] X.-Q. Li and Y. Arakawa, Phys. Rev. A **63**, 012302 (2000).
[3] Y. H. Huo, B. J. Witek, S. Kumar, J. R. Cardenas, J. X. Zhang, N. Akopian, R. Singh, E. Zallo, R. Grifone, D. Kriegner *et al.*, Nat. Phys. **10**, 46 (2013).
[4] P. Zanardi and F. Rossi, Phys. Rev. Lett. **81**, 4752 (1998).
[5] P. Michler, A. Kiraz, C. Becher, W. V. Schoenfeld, P. M. Petroff, L. Zhang, E. Hu, and A. Imamoglu, Science **290**, 2282 (2000).
[6] P. V. Kamat, J. Phys. Chem. Lett. **4**, 908 (2013).
[7] J. Tian and G. Cao, J. Phys. Chem. Lett. **6**, 1859 (2015).
[8] J. Xiang, W. Lu, Y. Hu, Y. Wu, H. Yan, and C. M. Lieber, Nature (London) **441**, 489 (2006).
[9] J. Kwak, W. K. Bae, D. Lee, I. Park, J. Lim, M. Park, H. Cho, H. Woo, D. Y. Yoon, K. Char, S. Lee, and C. Lee, Nano Lett. **12**, 2362 (2012).
[10] Y. Cui, Q. Wei, H. Park, and C. M. Lieber, Science **293**, 1289 (2001).
[11] Y. Shang and Z. Ning, Natl. Sci. Rev. **4**, 170 (2017).
[12] C. Delerue and M. Lannoo, *Nanostructures: Theory and Modeling* (Springer, Berlin, Germany, 2004).
[13] M. L. Cohen and T. K. Bergstresser, Phys. Rev. **141**, 789 (1966).
[14] J. R. Chelikowsky and M. L. Cohen, Phys. Rev. B **14**, 556 (1976).
[15] L.-W. Wang and A. Zunger, J. Chem. Phys. **100**, 2394 (1994).
[16] M. O. Steinhauser, *Computational Multiscale Modeling of Fluids and Solids: Theory and Applications* (Springer, Berlin, Germany, 2017).
[17] G. Bastard, *Wave Mechanics aApplied to Semiconductor Heterostructures* (Editions de Physique, Les Ulis, France, 1996).
[18] L. W. Wang and A. Zunger, J. Phys. Chem. **98**, 2158 (1994).
[19] J. R. Cárdenas and G. Bester, Phys. Rev. B **86**, 115332 (2012).
[20] J. R. Cárdenas, Superlattices Microstruct. **100**, 548 (2016).
[21] T. Puangmali, M. Califano, and P. Harrison, Phys. Rev. B **78**, 245104 (2008).
[22] A. Molina-Sánchez, A. García-Cristóbal, and G. Bester, Phys. Rev. B **86**, 205430 (2012).
[23] L.-W. Wang and A. Zunger, Phys. Rev. B **53**, 9579 (1996).
[24] P. A. Graf, K. Kim, W. B. Jones, and L.-W. Wang, J. Comput. Phys. **224**, 824 (2007).
[25] L.-W. Wang and A. Zunger, Phys. Rev. B **51**, 17398 (1995).
[26] C.-Y. Yeh, S. B. Zhang, and A. Zunger, Phys. Rev. B **50**, 14405 (1994).
[27] R. N. Sajjad and K. Alam, J. Appl. Phys. **105**, 044307 (2009).
[28] J. Kim and M. V. Fischetti, J. Appl. Phys. **110**, 033716 (2011).
[29] B. Delley and E. F. Steigmeier, Appl. Phys. Lett. **67**, 2370 (1995).
[30] T. Vo, A. J. Williamson, and G. Galli, Phys. Rev. B **74**, 045116 (2006).
[31] T. Sakurai and H. D. Hagstrum, Phys. Rev. B **12**, 5349 (1975).
[32] X. Gonze, J.-M. Beuken, R. Caracas, F. Detraux, M. Fuchs, G.-M. Rignanese, L. Sindic, M. Verstraete, G. Zerah, F. Jollet *et al.*, Comput. Mater. Sci. **25**, 478 (2002).
[33] J. A. Nelder and R. Mead, Comput. J. **7**, 308 (1965).
[34] R. O'Neill, J. R. Stat. Soc. C **20**, 338 (1971).
[35] K. M. Ho, M. L. Cohen, and M. Schlüter, Phys. Rev. B **15**, 3888 (1977).
[36] M. van Schilfgaarde, T. Kotani, and S. Faleev, Phys. Rev. Lett. **96**, 226402 (2006).